Thermodiffusion of CO_2 in Water by Nonequilibrium Molecular Dynamics Simulations

Felipe M. Coelho, Luís F. M. Franco, and Abbas Firoozabadi*

Cite This: *J. Phys. Chem. B* 2023, 127, 2749−2760

Read Online

ACCESS | 📊 Metrics & More | 📖 Article Recommendations | 🔳 Supporting Information

ABSTRACT: The components of a fluid mixture may segregate due to the Soret effect, a coupling phenomenon in which mass flux can be induced by a thermal gradient. In this work, we evaluate systematically the thermodiffusion of the CO_2−H_2O mixture, and the influence of the geothermal gradient on CO_2 segregation in deep saline aquifers in CO_2 storage. The eHeX method, a nonequilibrium molecular dynamics simulation approach, is judiciously selected to simulate the phenomenon. At 350 K, 400 bar, and CO_2 mole fraction of 0.02 (aquifer conditions), CO_2 accumulates on the cold side, and the thermal diffusion factor is close to 1 in a number of force fields. The lower the temperature, the higher is the separation and the thermal diffusion factor. In colder regions, water self-association is stronger, whereas the CO_2−H_2O cross-association and the CO_2−CO_2 interactions

enhance at higher temperatures. Thermodiffusion and gravitational segregation have opposite effects on CO_2 segregation. At typical subsurface conditions, the Soret effect is more pronounced than gravity segregation, and CO_2 concentrates in the top (colder region). Our work sets the stage to model the effect of electrolytes on CO_2 segregation in subsurface aquifers and other areas of interest.
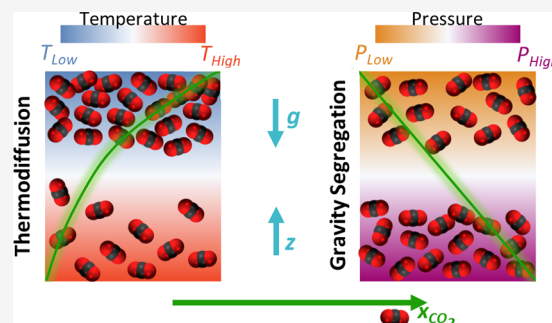
■ INTRODUCTION

The climate change and the ocean acidification are both caused by the rising carbon dioxide concentration in the atmosphere. A pH reduction in oceans has been reported in many regions, and the trend for the next decades is expected to be more severe.[1] Ocean acidification alters the local chemical speciation and creates conditions that impact marine life directly.[2] Carbon capture and storage (CCS) is one of the more promising methods to reduce CO_2 emissions to the atmosphere. In CCS, CO_2 is captured from an industrial source and injected into a formation, where it will be isolated from the atmosphere. The main feasible options for long-term storage of CO_2 are deep saline aquifers, depleted oil and gas reservoirs, and deep coal seams.[3]

There are several mechanisms that keep CO_2 in the subsurface. In structural trapping, CO_2 is physically restricted by an impermeable caprock. In dissolution trapping, CO_2 dissolves in formation brine, and, because the CO_2−brine mixture has a higher density,[4] the process is accelerated by convective mixing when the permeability is high. In residual trapping, CO_2 is trapped as bubbles in the pore space by capillary forces, interacting with the rock walls. In long-term mineral entrapment, CO_2 reacts with the host rock and the local fluid, precipitating as carbonates.[5,6]

In the long term, different nonconvective transport processes, such as Fickian diffusion, thermodiffusion, and gravitational segregation, could affect CO_2 distribution in subsurface aquifers. The driving forces for the above process

are the gradients of concentration, temperature, and pressure, respectively. In formations with an ideal liquid, gravitational segregation and thermodiffusion usually induce opposite effects in the species distribution: the lighter component tends to accumulate in the bottom (hotter region) due to thermodiffusion but in the top due to gravity segregation.[7]

Recently, Li et al.[5] have reported that the nonconvective transport redistribution time scale is around 10^5 years per meter for CO_2 in water, which indicates that the process is extremely slow compared with convective transport.[5] A simplified thermodynamic model for local equilibrium is employed to describe the fluid system, including an approximation for constant CO_2 activity coefficient. However, CO_2−H_2O is a nonideal fluid mixture, and there may be cross-association between the species.[8] Li et al.[5] conclude that, at steady state, CO_2 accumulates in the bottom due to gravitational segregation. They also state that, in nonisothermal conditions, the temperature effect on solubility gradient reduces the CO_2 concentration gradient. The mass flux

generated by the geothermal gradient from thermodiffusion is, however, neglected by Li et al.[5]

When a system is out of equilibrium, the principles of nonequilibrium thermodynamics define the process. From the local entropy production rate and the phenomenological laws,[9] the molar flux J_i for component i in a mixture with N_C components for $i = 1, 2, ..., N_C - 1$ is given by[10,11]

$$J_i = -c\left(\sum_j^{N_C-1} D_{ij}^M \nabla x_j + x_i x_N D_i^T \nabla T + D_i^P \nabla P\right) \tag{1}$$

where T, P, and x_i are the absolute temperature, pressure, and mole fraction of component i, respectively, c is the molar density, and D_{ij}^M, D_i^T, and D_i^P are the Fickian, thermal, and pressure diffusion coefficients. For a binary mixture with no chemical reaction, no external forces, and no viscous flow, eq 1 may be simplified to[10,11]

$$J_1 = -cD_{12}\left[\Gamma\nabla x_1 - \frac{x_1(1 - x_1)\alpha_{T,1}}{T}\nabla T - \frac{x_1}{RT}\left(\overline{V}_1 - \frac{M_1}{\rho}\right)\nabla P\right] \tag{2}$$

$$\Gamma = \left(\frac{\partial \ln f_1}{\partial \ln x_1}\right)_{T,P} \tag{3}$$

where D_{12} is the transport diffusion coefficient (Maxwell–Stefan diffusivity), ρ is the mass density, $\overline{V}_1$, and M_1 are the partial molar volume and the molecular weight of component 1, respectively, and R is the universal gas constant. At steady state conditions ($J_i = 0$), a concentration profile of the component i may be established because of a temperature gradient (thermodiffusion or Soret Effect) or a pressure gradient (pressure diffusion). The thermodynamic factor Γ in eq 3 is applied because diffusion is driven by the chemical potential (or the fugacity f_i) gradient, instead of the concentration directly.

The thermal diffusion factor, $\alpha_{T,i}$ quantifies the Soret effect, and can be related to the thermal diffusion coefficient ($D_1^T = \alpha_{T,1}D_{12}/T$). In an isobaric system at steady state condition for a binary mixture, the thermal diffusion factor can be defined as

$$\alpha_{T,i} = \Gamma\alpha_{T,i}^{Id} = -\Gamma\frac{T}{x_i(1 - x_i)}\frac{dx_i}{dT} \tag{4}$$

In past studies, only the so-called ideal thermal diffusion factor ($\alpha_{T,i}^{Id}$) has been computed, by assuming $\Gamma = 1$, even for nonideal fluids. When we approach the critical point, the thermodynamic factor approaches zero, and, unless the composition segregation increases, there will be a non-negligible reduction in $\alpha_{T,i}$, which is not captured by the assumption of $\Gamma = 1$. The thermal diffusion factor can be split into a physical contribution (represented by the mass and moment of inertia of the molecules) and a chemical contribution (represented by the interaction of the molecules, which may even lead to α_T sign alteration by concentration change depending on the mixture ideality).[12,13] For simple molecules, the physical contribution may adequately describe the phenomenon. Usually, the lighter component enriches on the hot side and the heavier on the cold side. This configuration allows a more effective heat conduction, because the contribution in heat flux is predominantly flux of kinetic energy for the lighter component, and intermolecular energy transfer for the heavier component.[14] In nonideal mixtures, the chemical effect may be dominant, and the theoretical description becomes complex.[15] Indeed, the real nature of the Soret effect remains largely unknown, and the complexity increases with associating species, such as the CO_2–H_2O mixture.[16,17]

There have been two attempts to measure the thermal diffusion factor of the CO_2–H_2O mixture. Windisch et al.[18] applied spatially resolved deep-ultraviolet (UV) Raman spectroscopy to quantify the concentration gradient of CO_2 due to a temperature gradient within a temperature range between 288 and 318 K and at pressures to 10 MPa. Below the saturation, they did not observe detectable Soret effect, within the uncertainty of the measurements ($|\alpha_{T,CO_2}^{Id}| < 9$). Guo et al.[19] have also performed experiments using UV Raman spectroscopy in a temperature gradient established between 295 and 353 K and pressures of 20 and 30 MPa. A saturated mixture of CO_2 was examined, and a concentration profile was observed, with CO_2 accumulating in the cold region. The authors conclude that the thermodynamic contribution (solubility) is dominant, and the kinetic effect (thermodiffusion) may be negligible. Nevertheless, they still computed the thermal diffusion coefficient for a wide range of temperature and pressure conditions by using a solubility model. Guo et al.[19] have obtained sharp variations of the thermal diffusion factor at higher temperatures, which may relate to the solubility and not to the Soret effect itself.

To investigate thermodiffusion, molecular simulation techniques, such as classical molecular dynamics (MD) simulations, can be applied. Statistical mechanics provides adequate tools to connect microscopic structures and mechanisms from MD simulations to macroscopic properties. The computations are based on the trajectory of the particles, obtained by integrating Newton's equation of motion, and the use of a force field to represent the interaction potential between particles. Molecular dynamics simulations have been employed to compute thermodiffusion in systems containing hydrocarbons,[20−25] Lennard-Jones fluids,[14,21,26−28] confined fluids,[7,29,30] associating liquids,[15,31−33] electrolytes in aqueous solution,[34−37] and silicate liquids.[38]

The Soret effect can be modeled using Boundary-Driven Nonequilibrium Molecular Dynamics (BD-NEMD) techniques.[12] A heat flux or a temperature gradient is generated in the simulation box, and a concentration profile is established by the system response, and then the thermal diffusion factor is computed directly from eq 4. To generate the heat flux, techniques such as the heat-exchange algorithm (HeX) or the momentum-exchange algorithm (PeX) are used. In the PeX, the momentum of the particle with the highest kinetic energy on the cold side is switched to the momentum of the particle with the same mass and the lowest kinetic energy from the hot side.[39] The heat flux in the HeX method is generated by adding kinetic energy in the hot region (by scaling the velocities of each particle), and by removing the same amount of kinetic energy in the cold side.[14] The temperature gradient can also be generated directly by applying thermostats, such as Langevin, in specific regions of the simulation box, and creating the heat flux as a consequence.[35]

In this work, we evaluate the thermodiffusion of CO_2 in water using nonequilibrium molecular dynamics techniques. Two of the available methods used widely are compared in simulations of the Ar–Kr mixture. From the comparison, the selected method is validated with experimental data for a liquid mixture of *n*-pentane and *n*-decane (C_5–C_{10}). Then, the Soret effect for CO_2–H_2O mixture is computed. Finally, the CO_2 distribution in typical geological conditions is quantified based on both thermodiffusion and gravitational segregation phenomena.

■ METHODS

Simulation Details. We first examine two different BD-NEMD simulation methods: eHeX and Langevin. In both, two regions are defined in the simulation box: a hot region where an energy source is applied, and a cold region where the energy is removed. These regions are located in such a way that they are not in direct contact with each other in the periodic image, as illustrated in Figure 1.
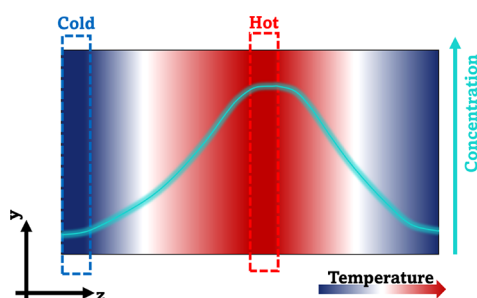

Figure 1. Representation of the simulation box with cold and hot regions and a schematic representation of concentration profile for a hypothetical thermophilic component.

The eHeX method is an enhanced version of the HeX, developed to reduce the drift in total energy due to truncation errors.[40] The velocities of the particles inside the hot and cold regions are scaled up and downward, respectively, and then shifted (to conserve the total momentum), creating a kinetic energy difference between the two regions.[14] In the Langevin method, the temperature of these two regions is fixed by a Langevin thermostat, which represents a heat bath with an implicit solvent, by adding an extra friction term in the equations of motion.[41]

In both methods, an amplified temperature gradient ($\sim 10^{10}$ K·m^{-1}) is imposed on the system to magnify the signal and establish a concentration profile in a reasonable simulation time. Provided that a linear profile for temperature is established, the local equilibrium condition is met, and the thermal diffusion factor can be computed.[42]

To model the interactions between atoms in the system, a force field is selected. The nonbonded interactions account for the van der Waals and electrostatics interactions, which may be expressed through the Lennard-Jones (LJ) and Coulombic potential, respectively, as

$$U_{ij}(r_{ij}) = 4\varepsilon_{ij}\left[\left(\frac{\sigma_{ij}}{r_{ij}}\right)^{12} - \left(\frac{\sigma_{ij}}{r_{ij}}\right)^{6}\right] + \frac{q_i q_j}{4\pi\epsilon_0 r_{ij}} \tag{5}$$

where the interaction potential U_{ij} between atoms i and j depends on the distance r_{ij} of the atoms, the depth ε_{ij} of the LJ interaction potential, the position σ_{ij} where the LJ interaction potential is zero, the vacuum permittivity ϵ_0 and the atom partial charge q_i. Unless differently specified, the LJ cross interactions parameters are derived from Lorentz–Berthelot (LB) combining rules ($\sigma_{ij} = (\sigma_{ii} + \sigma_{jj})/2$ and $\varepsilon_{ij} = \sqrt{\varepsilon_{ii}\varepsilon_{jj}}$).

All simulations are performed in LAMMPS.[43] First, an *NVT* equilibration is performed to keep the system close to the desired mean temperature, and then, the NEMD method is turned on. In the eHeX method, the velocities are scaled at each time step, and the scaling factor is chosen to guarantee the specified temperature gradient. In the Langevin method, initially a damp factor of 50 fs is used, and the temperature choice in the cold and hot regions is made based on the specified temperature gradient.

The temperature and the composition along the *z*-axis direction (which is the same direction as the temperature gradient) are computed by dividing the simulation box into 32 slabs (the hot and cold regions represent 2 slabs each). The thermal diffusion factor for each side of the box is then computed from eq 4 by analyzing the temperature and composition gradients, excluding the hot and cold regions and their adjacent slabs. The error is evaluated by performing 5 independent simulations for each set of conditions.

Ar–Kr System. A simple mixture of argon and krypton, which has no electrostatic interactions, is selected for comparison of the two methods. The force field parameters are shown in Table 1.[21]

Two sets of conditions are analyzed and compared with past MD results.[21,26] In the first, the system is an equimolar mixture with a total of 500 atoms arranged in a cubic box with a density of 1910 kg·m^{-3}, with a mean temperature around 116 K, and the temperature difference between cold and hot regions around 50 K. In the second, an orthorhombic box is set with the size in direction z (L_z) twice as long as the other directions, and the argon composition (mole fraction), density, and temperature of 0.68, 1810 kg·m^{-3}, and 95 K, respectively. In the second mixture, the system size and temperature gradient dependencies are evaluated. For all systems, the cutoff in LJ interactions and the time step are set to 0.8 nm and 1 fs, respectively. The *NVT* equilibration is set for 200 ps, followed

Table 1. Force Field Parameters for the Atoms and Pseudoatoms in All Simulations[a]

					SPCE		TIP4P/2005[b]		EPM2		TraPPE	
atom	Ar	Kr	CH$_2$	CH$_3$	O$_w$	H$_w$	O$_w$	H$_w$	C$_c$	O$_c$	C$_c$	O$_c$
σ (nm)	0.341	0.363	0.395	0.375	0.317	0	0.316	0	0.276	0.303	0.280	0.305
ε/k_b (K)	120	167	46	98	78.2	0	93.2	0	28.1	80.5	27.0	79.0
q (e)	0	0	0	0	−0.8476	0.4238	−1.1128	0.5564	0.6512	−0.3256	0.700	−0.3500

[a]The subscripts *w* and *c* represent the H_2O and CO_2 molecule, respectively. [b]The negative charge is in a massless site located 0.1546 Å from O in the interior bisector of H–O–H.

by initially 100 ns with the NEMD method (in the second set of conditions, the simulation time is chosen based on the analysis of the first one), where the first 5 ns entails the method equilibration. For this mixture, $\alpha_{T,i} = \alpha_{T,i}^{Id}$, since it could be fairly well described as a mixture of ideal gases, and as a consequence $\Gamma = 1$.

C_5-C_{10} *System.* The second system for the method validation is a mixture of *n*-pentane (C_5) and *n*-decane (C_{10}). A united-atom model (TraPPE) is chosen to represent the interaction potential,[44] where hydrogens atoms are implicitly embedded in the groups CH_2 and CH_3, for which the LJ parameters are presented in Table 1. The bonded potentials are included to represent bond stretching, bond-angle bending, and torsion.

To compare with experimental data from Perronace et al.,[26] an equimolar and a $x_{C5} = 0.8$ mixture are simulated with a mean temperature of 300 K in both, and density of 688 and 652 kg·m^{-3}, respectively (close to the experimental density for atmospheric pressure condition[24]). The orthorhombic ($L_z:L_y:L_x = 2:1:1$) simulation box containing 2000 molecules is equilibrated for 1 ns, and then the method is turned on for 100 ns, with a temperature difference between the thermostatized regions of 72 K. A cutoff distance of 1.4 nm and a time step of 2 fs are used. To evaluate the nonideality of the system, the thermodynamic factor is computed using the Peng–Robinson equation of state.[45]

CO_2-H_2O *System.* For the CO_2-H_2O system, different combinations of force fields are selected to investigate the sensitivity of the results. First, the system is represented by the SPCE water[46] and the EPM2 CO_2[47] semiflexible models, with constraint in the bonds, but with a harmonic potential in the angles.[48] The TraPPE[49] and TIP4P/2005[50] model for CO_2 and water, respectively, are also analyzed.[51,52] The force field parameters for each model are presented in Table 1. The LB combining rules are used; however, for the SPCE-EPM2[48] and SPCE-TraPPE[52] combinations, and optimized cross-interaction parameters based on phase behavior of the mixture are used as shown in Table 2.

Table 2. Optimized LJ Cross-Interaction Parameters for the Optimized CO_2-H_2O Force Field Combinations[48,52]

force fields	σ_{C,O_w} (nm)	σ_{O,O_w} (nm)	$\varepsilon_{C,O_w}/k_b$ (K)	$\varepsilon_{O,O_w}/k_b$ (K)
SPCE-EPM2	0.284	0.315	66.3	90.1
SPCE-Trappe	0.306	0.305	53.0	79.1

The simulation box is set with 1000 molecules randomly placed within a region with the proportion $L_z:L_y:L_x$ of 2:1:1, and a density of 1000 kg·m^{-3}. The CO_2 composition in mole fraction is set at 0.02, a value below the solubility for the pressure and temperature studied, to avoid phase separation. The mean temperature and the temperature difference between the cold and hot regions are 350 K and 50 K, respectively.

Electrostatics and LJ interactions are calculated directly within 1 nm from each atom. Beyond 1 nm, the long-range electrostatic interactions are computed applying the particle–particle/particle–mesh (PPPM) algorithm.[53] The Rattle algorithm is used for the constraints, and the degree of freedom in temperature calculation is corrected accordingly.[54] The *NVT* equilibration is set for 1 ns, followed by 80 ns with the NEMD method, from which the last 75 ns are used to compute properties.

In the CO_2-H_2O mixture, the thermodynamic factor is computed from equilibrium molecular dynamics (EMD) simulations and the Cubic Plus Association (CPA) equation of state[55] (more details below), to obtain the thermal diffusion factor. The thermodynamic factor from MD is computed through the Kirkwood–Buff integrals (KBI) using the method from Dawass et al.[56] to account for the finite size of the system. Details are described in the Supporting Information.

Gravity Segregation. When a system is subjected to a gravitational field, the chemical potential for each component becomes a function of the height z (here, z is in the same direction, but opposite orientation, as the gravitational field). The gravity may establish a concentration gradient in the system, even at equilibrium conditions. The mechanical equilibrium is also modified once the gravitational field leads to a hydrostatic pressure gradient ($\nabla P = -\rho g$). For a binary nonisothermal system, the fugacity variation of component i for $i = 1, 2, ..., N_C$ can be expressed by

$$\left(\frac{\partial \ln f_i}{\partial z}\right)_T = -\frac{M_i g}{RT} - \frac{(1 - x_i)\alpha_{T,i}}{T}\left(\frac{dT}{dz}\right) \tag{6}$$

where g is the gravity acceleration.[11]

To evaluate the influence of gravitational segregation on the CO_2-H_2O system, the Peng–Robinson Cubic-Plus-Association (PR-CPA) Equation of State (EoS) is used. The CPA has an additional term to account for the association between molecules. The CPA has been applied to water-containing systems to account for the highly directional hydrogen bonds.[57−59] The CO_2-H_2O phase behavior has also been described, and it has been found that, although CO_2 molecules do not self-associate, cross-association with water molecules through the solvation layer is non-negligible.[8]

The CO_2 and the H_2O molecules are modeled as a 4-site association scheme: 2 α hydrogen-bond donors and 2 β hydrogen-bond acceptors.[60] The association or cross-association for each molecule can be evaluated through the χ_i parameter, which is the component mole fraction not associating with any other site from another molecule, either H_2O-H_2O association or CO_2-H_2O cross-association. Details of the PR-CPA equations, the fugacity coefficient, and the validation for the CO_2-H_2O mixture are provided in the Supporting Information. The parameters for the CO_2-H_2O mixture are taken from Li and Firoozabadi.[8]

The gravitational segregation is evaluated in both isothermal and nonisothermal conditions, and compared with the thermodiffusion without gravity. Then, we analyze the CO_2 distribution for each one of the cases for a formation with 500 m of thickness.[61] The formation bottom is set at 350 K, 400 bar, and $x_{CO_2} = 0.02$, and a constant temperature gradient of -30 K·km^{-1} is applied for the nonisothermal case, which is typical for the geothermal gradient.[19,62]

RESULTS AND DISCUSSION

Validation of BD-NEMD. The temperature and concentration profile for the first set of conditions for the Ar–Kr mixture are shown in Figure 2. For both methods, a linear temperature profile within the box is established, which is consistent with the local equilibrium condition. The temperature standard deviation in the eHeX method is higher than in the Langevin, because the final temperature profile in eHeX depends on the local instantaneous temperature of the equilibration final step, whereas in the Langevin method the
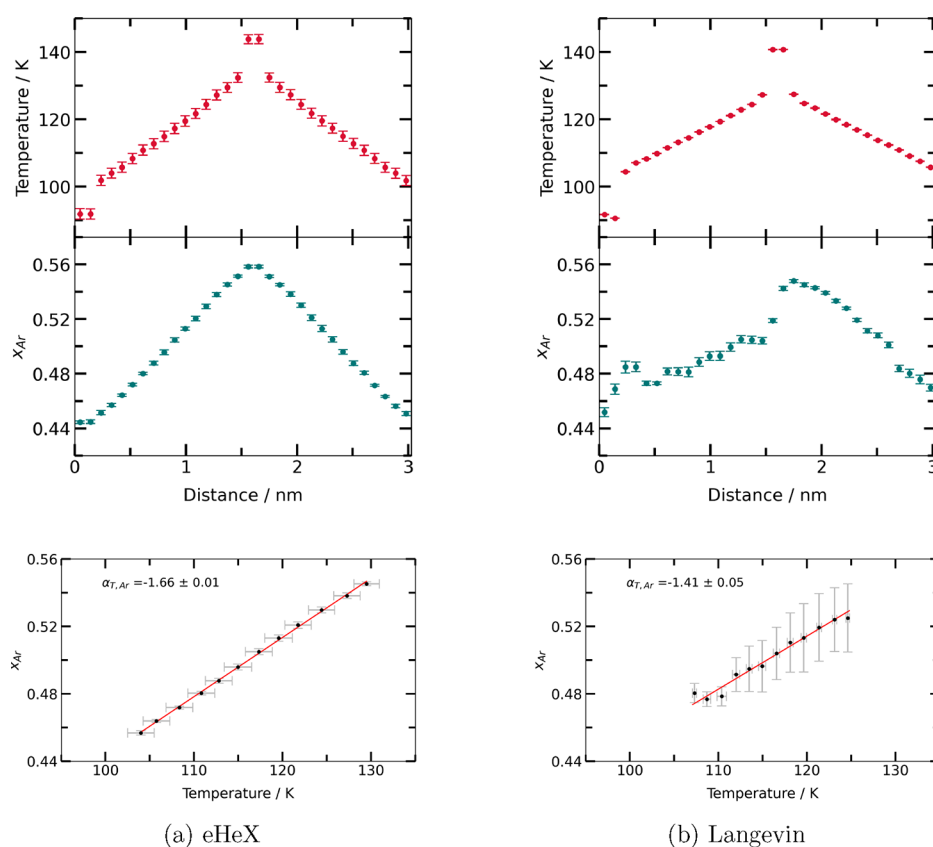
Figure 2. Temperature and argon composition profile in the simulation box, and the concentration dependency on temperature: (a) eHex and (b) Langevin methods at $T = 116$ K, $\rho = 1910$ kg·m^{-3}, $x_{Ar} = 0.50$, and $N = 500$ atoms.
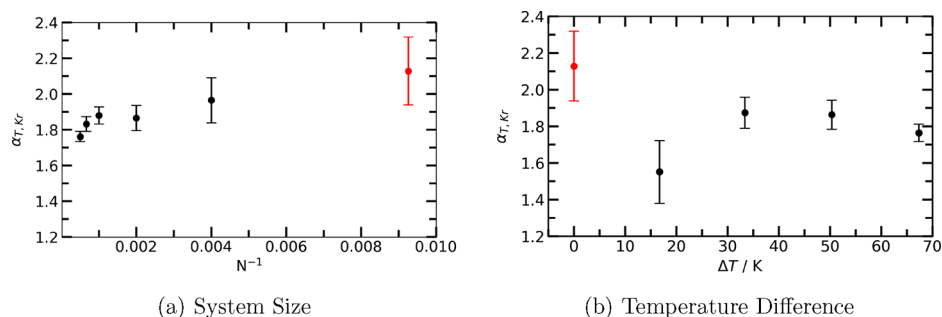

Figure 3. Influence of (a) system size ($\Delta T = 50$ K and $L_z = 4.6$ nm) and (b) temperature difference between hot and cold regions ($N = 500$ atoms and $L_z = 4.6$ nm) on the Ar−Kr thermodiffusion at $T = 95$ K, $\rho = 1810$ kg·m^{-3}, and $x_{Ar} = 0.68$. The result from the EMD method[26] is in red.

thermostat fixes the temperature in those regions during the simulation. In both methods, argon tends to accumulate in the hot region, because it is the lighter component.[14] While the concentration profile for eHeX is linear and symmetrical ($\alpha_{T,Ar}$ = −1.66 ± 0.01), for Langevin it is not ($\alpha_{T,Ar}$ = −1.41 ± 0.05). Although the mean values for both methods are similar, the concentration dispersion is smaller in eHeX. From past MD studies using both the BD-NEMD and EMD,[14,21,27] the average $\alpha_{T,Ar}$ is −1.78 (Figure S3 in Supporting Information), which is closer to the eHeX result. Overall, eHeX is more accurate.

The nonlinearity in the Langevin profile persists by increasing the system size (2000 atoms) and simulation time (200 ns). However, the linearity and symmetry are enhanced by increasing the damp factor, initially at 50 fs, to 250 and 500 fs (Figure S4 in Supporting Information). If the thermostat acts too often on the system, the molecular dynamics will be

disturbed, and the steady state established will not be correct. Nevertheless, increasing the damp factor reduces the temperature difference between the hot and cold regions, because the system tries to reach thermal equilibrium in between the thermostat action. The eHeX is chosen as the standard method for the rest of our work.

For the second set of Ar−Kr conditions, the simulations are run for 40 ns, and the influence of the temperature gradient and the system size is analyzed (Figure 3). The results are also compared with the EMD simulations from past studies.[26] Usually, the EMD technique does not provide good statistics due to dependency on equilibrium oscillations. Perronace et al.[26] have used only 108 atoms in their simulations, which amplifies the uncertainties.

The larger the system size and the temperature gradient, the higher is the accuracy and the faster the convergence for a fixed simulation time. By increasing these parameters, the signal is

magnified, and a shorter simulation time is required to obtain good statistics. On the other hand, increasing the system size also affects the simulation speed, whereas, with large temperature gradients, the analysis of the temperature dependency on the Soret effect becomes more difficult, and local phase transitions may occur.

In the C_5–C_{10} system, the thermodynamic factor is evaluated using the Peng–Robinson equation of state (Figure S5 in the Supporting Information) at 300 K and 1 bar. Because the deviation from ideality is always less than 1%, we assume $\alpha_{T,C_5} = \alpha_{T,C_5}^{Id}$. Then, α_{T,C_5} and the error from the simulations sampling are computed by the eHeX method (temperature and concentration plots in Figure S6 in the Supporting Information). The lighter component (C_5) accumulates on the hot side, following what would be expected for an ideal liquid. Finally, the results are compared with past MD simulations (HeX method) and experimental data[20] (Figure 4).
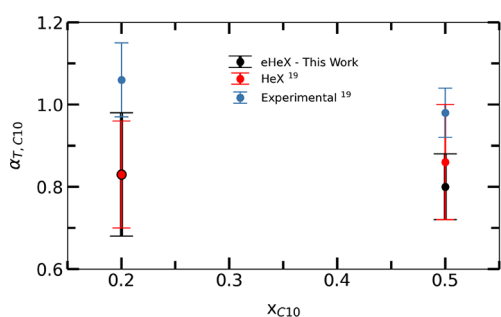

Figure 4. Thermal diffusion coefficient and standard deviation for two C_{10} compositions (0.2 and 0.5 in mole fraction) compared with past MD simulations and experimental data,[20] at T = 300 K, $P \approx 1$ bar, and N = 2000 molecules.

The thermal diffusion factor for the HeX and eHex methods are similar for the two sets of concentrations, but they both underestimate the experimental data by a factor of around 20%. The large standard deviation could be reduced by increasing the system size, the simulation time, or the number of independent simulations in the sampling. In the eHeX from this work and in the HeX from Perronace et al.,[20] a united-atom model has been used as the force field. The use of LB combining rules could be inadequate to represent united-atom models, and an adjustable parameter for the cross-energy parameter may be required.[63,64] This could be the reason for a systematic deviation from experimental data. However, based on the thermodynamic factor, C_5–C_{10} behaves as an ideal liquid, and the intermolecular interactions should not be as relevant. Hence, the bonded interactions must be dominant in the Soret effect behavior, especially the torsion due to its relation with the molecules moment of inertia. Nevertheless, the use of such a simplified force field yields results close enough to experimental values. The eHex method has been also applied to simulate the system at the same condition using

the same force field by Antoun et al.[24] The reported values of $\alpha_{T,C_{10}}$ (0.98, and 0.94, for $x_{C_{10}}$ = 0.2 and 0.5, respectively) are closer to the experimental data than ours. However, based on the analysis of their concentration and temperatures profiles in the simulation box, the $\alpha_{T,C_{10}}$ values ($\approx$0.82, and 0.76, for $x_{C_{10}}$ = 0.2 and 0.5, respectively)[24] are far from the experimental data than the values from our work.

Soret Effect in CO_2–H_2O. The CO_2–H_2O system has challenges due to association and cross-association between molecules. A larger system is needed for accuracy because of low CO_2 concentration. Besides the bonded interactions, the particles have partial charge, and one needs to account for the electrostatic interactions. There will be a significant slowdown in the simulations compared to the Ar–Kr and C_5–C_{10} mixtures.

We observed energy drift higher than 20% in our preliminary 80 ns long simulations. Some energy drift[40] is expected, even in the classical microcanonical ensemble, but not that large. The energy drift is reduced to less than 0.1% by increasing the PPPM algorithm precision (desired relative error accuracy in forces from 10^{-4} to 10^{-5}), the electrostatic cutoff (from 1 to 1.2 nm), and the precision in the Rattle algorithm for the constraint bonds (desired accuracy tolerance from 10^{-4} to 10^{-10}).

The CO_2–H_2O thermodiffusion at T = 350 K, ρ = 1000 kg· m^{-3}, and x_{CO_2} = 0.02 is evaluated for various force fields (Table 3). The results change depending on the force field, but the trend is the same: CO_2 accumulates on the cold region ($\alpha_{T,CO_2}^{Id} > 0$), and the thermal diffusion factor is around 1 (the mean value is 1.08 and the largest deviation is 5.1%). Due to the similarity of the results in various force fields, only the conventional SPCE + EPM2 combination will be presented.

From the temperature and concentration profiles for the selected force field (Figure S7 in Supporting Information), the data are very scattered, resulting in a relatively large error (around 15%) for the thermal diffusion factor. To increase the accuracy, the system size is increased (fixing L_z = 5.0 nm to keep the same temperature gradient). By using 5000 molecules (100 CO_2 molecules and 4900 H_2O molecules) instead of 1000 (20 CO_2 and 980 H_2O molecules), the linearity and symmetry in concentration profile and the overall accuracy increase: α_{T,CO_2}^{Id} = 0.94 ± 0.04 (Figure 5).

An increase in the system size results in an increase in the CPU time. Figure 6 shows the effect of simulation time on the thermal diffusion factor for two system sizes. By increasing the simulation time both simulation sizes converge to the same result. For the 5000-molecule simulation with only 40 ns the convergence is close enough to the final result. In our next simulations, we will have 5000 molecules in the box and the simulation time will be 40 ns.

For the CO_2–H_2O mixture, CO_2 (the heavier component) accumulates in the cold region. Although CO_2–H_2O constitutes a nonideal mixture, its thermal diffusion exhibits the same behavior observed for ideal mixtures.[14] In past studies

Table 3. α_{T,CO_2}^{Id} for Various Force Field Combinations at T = 350 K, ρ = 1000 kg·m^{-3}, x_{CO_2} = 0.02, and N = 1000 Molecules[a]

SPCE + EPM2	TIP4P + TraPPE	SPCE + EPM2 (opt)	SPCE + TraPPE (opt)
1.03 ± 0.15	1.14 ± 0.06	1.13 ± 0.17	1.04 ± 0.16

[a]The term "opt" stands for optimized cross-interactions parameters for the mixture.
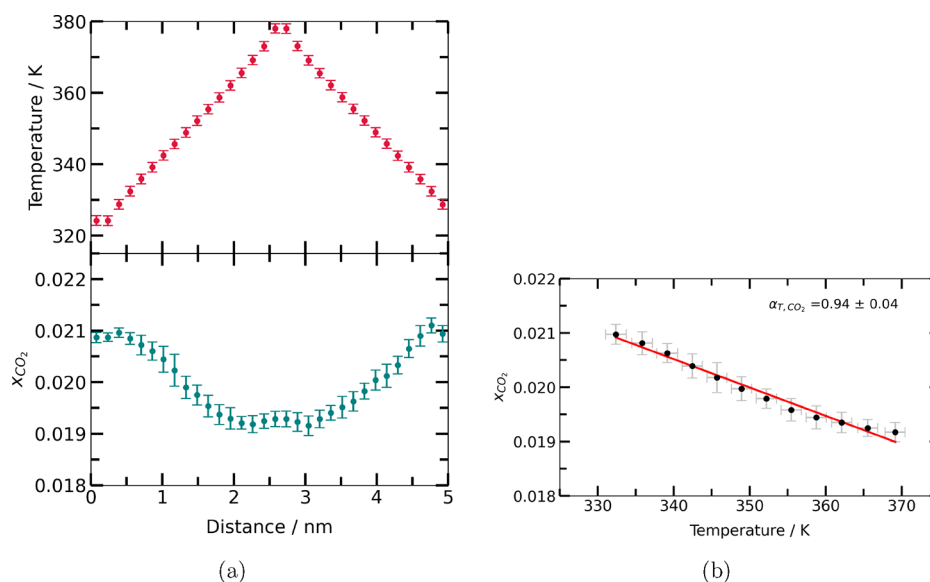
Figure 5. (a) Temperature and CO_2 composition profile in the simulation box, and (b) the concentration vs temperature at T = 350 K, ρ = 1000 kg·m^{-3}, x_{CO_2} = 0.02, and N = 5000 molecules.
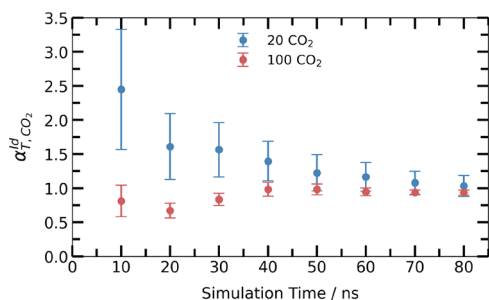

Figure 6. Ideal CO_2–H_2O thermal diffusion factor vs simulation time for N = 1000 (20 CO_2) and 5000 (100 CO_2) molecules at T = 350 K, ρ = 1000 kg·m^{-3}, x_{CO_2} = 0.02.

for other aqueous mixtures, the trend for an ideal liquid is also observed in water-rich compositions. However, by increasing the concentration of the nonwater component, the thermal diffusion factor sign changes and the heavier molecule enriches the hot region.[15]

The α_{T,CO_2}^{Id} dependency on temperature and pressure is also evaluated. All simulations are carried out in the canonical ensemble, which allows the pressure to fluctuate. The average pressure from the initial condition is around 400 bar. To evaluate the pressure dependency at the same mean temperature (350 K) the simulation box is equilibrated with a thermostat and an anisotropic barostat in the x and y direction (to keep the temperature gradient constant in the z direction). At 200 bar and 350 K, α_{T,CO_2}^{Id} = 0.68 ± 0.13. For temperature dependency evaluation at a fixed pressure (400 bar), the simulations are equilibrated with a thermostat and an anisotropic barostat. The thermal diffusion factor is then

evaluated at various mean temperatures keeping the temperature gradient constant (Table 4).

The thermodiffusion in the CO_2–H_2O mixture has a pronounced dependency on temperature. The thermal diffusion factor decreases by almost 50% by increasing the temperature from 300 to 350 K, whereas it decreases by 28% by decreasing the pressure from 400 to 200 bar. Overall, by increasing the temperature at a constant pressure the Soret effect is reduced, and at 400 K the effect is almost negligible.

To get molecular insights into temperature dependency, EMD simulations are performed at various temperatures (300, 350, and 400 K) at the same pressure (400 bar). The radial distribution function $g(r)$ is computed for water atoms ($g_{O_wH_w}(r)$), for CO_2 atoms ($g_{C_cO_c}(r)$), and between atoms of water and CO_2 ($g_{O_wC_c}(r)$ and $g_{H_wO_c}(r)$) (Figure 7).

Water molecules interact through highly directional hydrogen bonds, which are represented by the first sharp peak in Figure 7a. The hydrogen bond network is distorted and the peak decreased by increasing the temperature.[65] CO_2 molecules do not have a net dipole moment, but they interact through van der Waals and quadrupole–quadrupole interactions. For CO_2, the higher the temperature, the higher are these interactions. The cross-interactions between CO_2–H_2O molecules could be through O_w–C_c tetrel bonds or H_w–O_c hydrogen bonds (represented by the first shoulder highlighted in Figure 7d). From Figure 7, the tetrel bonds, in which CO_2 acts as an Lewis acid, are more significant than the weak hydrogen bonds for this mixture, in agreement with past studies.[66] A similar conclusion regarding these interactions has been recently made for the mixture of CO_2–H_2S.[67] The interaction via the tetrel bond is decreased by temperature, whereas the hydrogen bonds are slightly enhanced on the first

Table 4. Ideal Thermal Diffusion Factor of the CO_2–H_2O Mixture for 40-ns-Long Simulations at Various Mean Temperatures, P = 400 bar, x_{CO_2} = 0.02, and N = 5000 Molecules

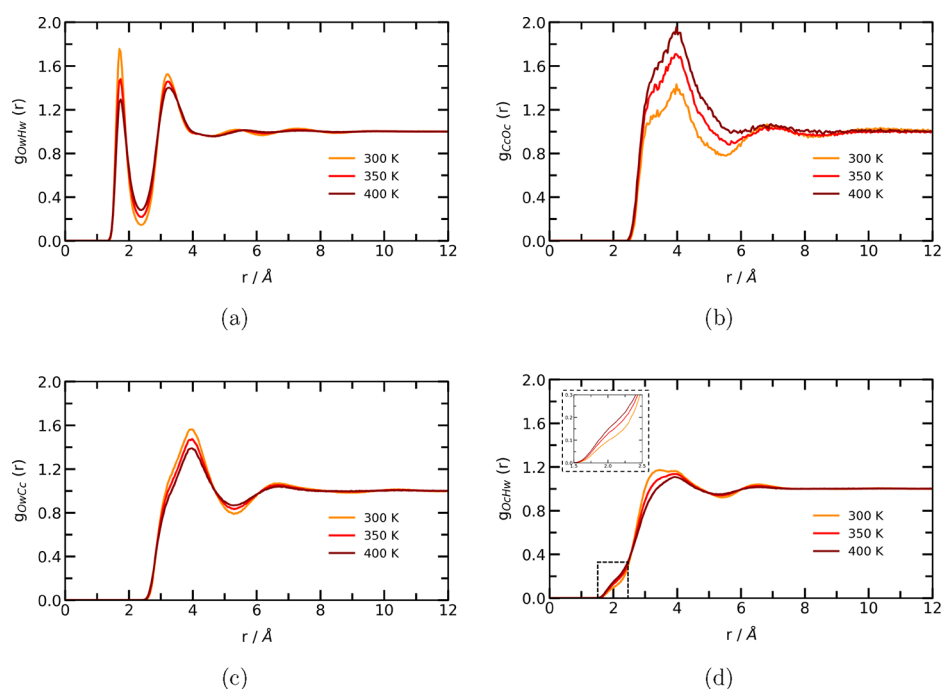| T/K	301.0 ± 0.4	321.2 ± 0.5	350.6 ± 0.6	381.0 ± 0.2	402.0 ± 0.2
α_{T,CO_2}^{Id}	1.85 ± 0.10	1.21 ± 0.08	0.98 ± 0.10	0.35 ± 0.12	−0.12 ± 0.17

Figure 7. Radial distribution functions, $g(r)$, between (a) oxygen and hydrogen atoms of water molecules, (b) carbon and oxygen atoms of CO_2 molecules, (c) water-oxygen and CO_2-carbon atoms, (d) water-hydrogen and CO_2-oxygen atoms at $P = 400$ bar, $x_{CO_2} = 0.02$, and $T = 300, 350$, and 400 K.

shoulder. A similar analysis is made to investigate the pressure dependency in those interactions. We observe no noticeable pressure effect (Figure S8 in the Supporting Information).

Overall the separation between CO_2 and water molecules due to a temperature gradient is enhanced by increasing the mixture density (lower temperature and higher pressure). CO_2 accumulates in the cold region where its interactions with other CO_2 molecules are reduced, whereas water accumulates in the hot region where it has reduced self-association.

To estimate the thermal diffusion factor from the diffusion driven by chemical potential gradient, the thermodynamic factor is computed at the above temperatures at 400 bar (Figure 8). The thermodynamic factor is a measure of the
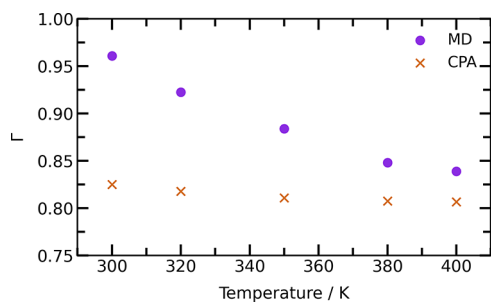

Figure 8. Thermodynamic factor of CO_2-H_2O mixture vs temperature from CPA EoS and MD simulations at $P = 400$ bar, $x_{CO_2} = 0.02$, and $N = 5000$ molecules.

nonideality of mixtures and provides an indication of the mixture stability ($\Gamma < 0$ indicates an unstable mixture). Figure 8 shows that the results from MD based on finite-size consideration get closer to the CPA EoS results at higher temperatures. The disagreement at lower temperatures is related to the short linear regime obtained in the Kirkwood–

Buff integral between CO_2 molecules, due to the low concentration of CO_2 in the mixture. By increasing the temperature, Γ is reduced, and at higher temperatures, a phase separation probably would occur and the thermodynamic factor would become negative.

Unlike the C_5-C_{10} mixture, the deviation from ideality in CO_2-H_2O mixture is non-negligible; it can be as high as 20% away from the ideal condition. The thermal diffusion factor is computed using eq 4. Considering only the dependency on temperature, a model for α_{T,CO_2} can be obtained by a linear interpolation (Figure 9). This model can then be used for a temperature range between 300 and 400 K and a pressure and CO_2 concentration of 400 bar and 0.02 in mole fraction, respectively.

CO_2-H_2O Segregation. The gravitational field contribution to the chemical potential could lead to a redistribution of CO_2 in deep saline aquifers. The calculated isothermal gravity segregation using the CPA EoS for CO_2-H_2O is shown in Figure S9 in the Supporting Information for various temper-
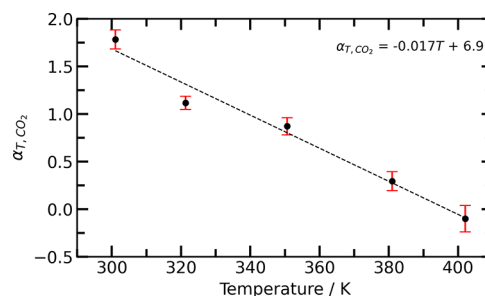

Figure 9. Thermal diffusion factor of CO_2-H_2O vs temperature at $P = 400$ bar, $x_{CO_2} = 0.02$, and $N = 5000$ molecules. The dashed line represents the linear interpolation.

atures. The equilibrium distribution of CO_2 is affected by the gravitational field, and the segregation depends on the temperature: the lower the temperature, the more pronounced is the effect. In general, CO_2 accumulates in the bottom of the formation, but by increasing the temperature this trend decreases and could be even reversed at higher temperatures. The hydrostatic pressure increases with depth; the denser mixture at lower temperatures enhances the pressure drop from the top to the bottom of the column.

CO_2 accumulation in the bottom due to gravitational segregation has been also reported by Li et al.[5] At similar conditions in the bottom (T = 348 K, P = 250 bar, and x_{CO_2} = 0.022) for a 500-m thick column, it is expected a CO_2 segregation of 1.4% by the CPA EoS, whereas Li et al. predicted a segregation of 1.7%. The assumption that the CO_2 activity coefficient is independent of composition may result in different segregation magnitudes.

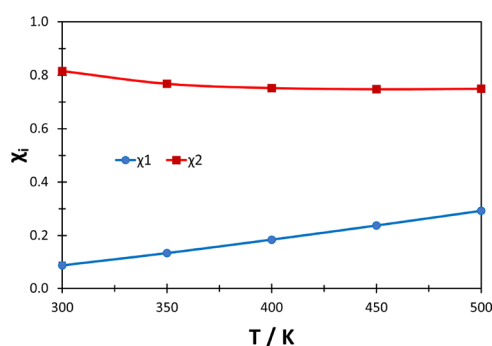To evaluate the association strength as a function of temperature, χ_i from the CPA EoS is computed (Figure 10).

Figure 10. Nonbonded mole fraction of H_2O with H_2O (χ_1) and CO_2 with H_2O (χ_2) molecules vs temperature from the CPA EoS at P = 400 bar and x_{CO_2} = 0.02.

The water self-association decreases with temperature, as concluded by MD simulations (Figure 7a). The cross-association, however, slightly increases from 300 to 350 K, and is almost constant at higher temperatures (similar to the hydrogen bond interactions highlighted in Figure 7d). Overall, the heavier molecule (CO_2) will tend to sink, even with the self-association of water molecules. The version of CPA used here does not account for the quadrupole interactions, which could lead to misleading results when these interactions are relevant.[68] A similar analysis is made in regards to the pressure dependency in these parameters, but, as in MD simulations, no noticeable effect is observed (Figure S10 in the Supporting Information).

Finally, the impact of both thermodiffusion (without a gravitational field) and gravity segregation (without a temperature gradient) and the combined effect are evaluated for typical subsurface conditions (Figure 11). The conditions at the bottom of the formation are 350 K, 400 bar, and x_{CO_2} = 0.02. The CO_2 composition for thermodiffusion is computed by integrating Eq. 4, using the thermal diffusion factor model developed from MD simulations, and a temperature gradient of −30 K·km^{-1}. The thermodiffusion has a trend opposite to gravity segregation: the gravitational field increases the concentration of CO_2 in the bottom, while the negative temperature gradient enhances its concentration in the top (the cold region). The thermal diffusion factor dependency on
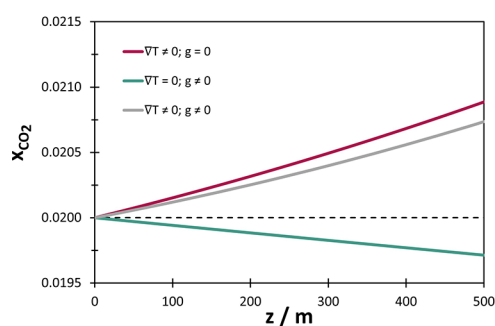
Figure 11. CO_2 composition distribution due to thermodiffusion (∇T = −30 K·km^{-1}, g = 0), gravity segregation (∇T = 0, g = 9.81 m·s^{-2}), and coupled phenomena (∇T = −30 K·km^{-1}, g = 9.81 m·s^{-2}) at T = 350 K, P = 400 bar, and x_{CO_2} = 0.02 in the bottom.

temperature becomes evident by the nonlinearity of the x_{CO_2} profile when $\nabla T \neq 0$, because the lower the temperature, the higher is the segregation. For this set of conditions, thermodiffusion is more pronounced than gravity segregation, and when both phenomena are coupled CO_2 accumulates on the top, with a CO_2 segregation estimated at 3.7% for a 500-m-thick formation.

There is a significant pressure change (around 12% for the 500-m-thick formation) that may decrease the overall thermal diffusion factor. In our work, we determine the expected CO_2 distribution in aquifers, but not the time required to reach the steady state; the estimated time scale for a complete redistribution for a 500-m formation can be as long as 50 million years if the Soret effect is not accounted for.[5] We do not take into account the effect of salts, which will be evaluated in future work. Nevertheless, we have studied for the first time the thermodiffusion of CO_2 in aqueous phase and compare it with the gravity segregation.

■ CONCLUSIONS

In recent years, boundary-driven nonequilibrium molecular dynamics (BD-NEMD) have been used to calculate thermodiffusion coefficients. In our work, we simulate the Soret effect in the Ar−Kr mixture using two different BD-NEMD methods: eHeX, and Langevin. We find that the eHeX method may provide more accurate results. The higher accuracy may be due to the direct generation of heat flux.

The focus of our work is the investigation of thermodiffusion of the CO_2−H_2O mixture at subsurface conditions. The main findings from our work are

1. Under temperature gradient, CO_2 accumulates in the cold region. As temperature increases, water self-association decreases, but CO_2 interactions and CO_2−H_2O cross-association increase. CO_2 molecules tend to accumulate where the hydrogen bond network is more established. The Soret effect for CO_2 in water is enhanced as density increases by decreasing the temperature or increasing the pressure. The temperature effect on the thermal diffusion factor is pronounced.

2. In the subsurface in a CO_2−H_2O liquid column, there is the effect of both the gravitational field and the geothermal gradient. We used the cubic-plus-association (CPA) EoS and the thermal diffusion factor from the NEMD simulations to obtain the CO_2 segregation. There is good agreement between CPA EoS and MD simulations in both the CO_2−H_2O structure and

thermodynamic factor ($\partial[\ln f_{CO_2}]/\partial[\ln x_{CO_2}]$). The non-convective transport phenomena have opposite trends: CO_2 accumulates at the bottom for gravity segregation and at the top for the Soret effect. For a typical geothermal gradient, the thermodiffusion effect is more pronounced than the gravity segregation effect and CO_2 will tend to accumulate at the top of the formation.

Salinity may also affect thermodiffusion in the CO_2–H_2O system. Hence, a continuation of this work will be the evaluation of the thermodiffusion of CO_2 in brine.

■ ASSOCIATED CONTENT

ⓢ Supporting Information

The Supporting Information is available free of charge at https://pubs.acs.org/doi/10.1021/acs.jpcb.2c08260.

Methodology to compute the thermodynamic factor from molecular dynamics; CPA-PR EoS and validation for the CO_2–H_2O mixture; comparison of the Ar–Kr thermal diffusion factor with previous MD studies; damp factor influence on the Langevin thermostat; thermodynamic factor and temperature and concentration profiles for the C_5–C_{10} mixture; temperature and concentration profile for the 1000-molecule system of the CO_2–H_2O system; CO_2 concentration and pressure profiles in isothermal gravity segregation; and pressure influence on the radial distribution functions and on the CPA association parameter for CO_2–H_2O (PDF)

■ AUTHOR INFORMATION

Corresponding Author

Abbas Firoozabadi − *Reservoir Engineering Research Institute (RERI), Palo Alto, California 94306, United States;* ⓞ orcid.org/0000-0001-6102-9534; Email: af@rerinst.org

Authors

Felipe M. Coelho − *School of Chemical Engineering, University of Campinas, Campinas, SP 13083-852, Brazil; Reservoir Engineering Research Institute (RERI), Palo Alto, California 94306, United States;* ⓞ orcid.org/0000-0002-7572-1991

Luís F. M. Franco − *School of Chemical Engineering, University of Campinas, Campinas, SP 13083-852, Brazil*

Complete contact information is available at:
https://pubs.acs.org/10.1021/acs.jpcb.2c08260

Notes

The authors declare no competing financial interest.

■ ACKNOWLEDGMENTS

■ REFERENCES

(1) Haugan, P. M.; Drange, H. Effects of CO_2 on the ocean environment. *Energy Convers. Manage.* **1996**, *37*, 1019−1022.

(2) Doney, S. C.; Fabry, V. J.; Feely, R. A.; Kleypas, J. A. Ocean acidification: The other CO_2 problem. *Annu. Rev. Mar. Sci.* **2009**, *1*, 169−192.

(3) Boot-Handford, M. E.; Abanades, J. C.; Anthony, E. J.; Blunt, M. J.; Brandani, S.; Mac Dowell, N.; Ferńandez, J. R.; Ferrari, M.-C.; Gross, R.; Hallett, J. P.; et al. Carbon capture and storage update. *Energy Environ. Sci.* **2014**, *7*, 130−189.

(4) Teng, H.; Yamasaki, A.; Chun, M.; Lee, H. Solubility of liquid CO_2 in water at temperatures from 278 to 293 K and pressures from 6.44 to 29.49 MPa and densities of the corresponding aqueous solutions. *J. Chem. Thermodyn.* **1997**, *29*, 1301−1310.

(5) Li, Y.; Orr, F. M.; Benson, S. M. Long-term redistribution of residual gas due to non-convective transport in the aqueous phase. *Transp. Porous Media* **2022**, *141*, 231−253.

(6) Zhang, X.; Ge, J.; Kamali, F.; Othman, F.; Wang, Y.; Le-Hussain, F. Wettability of sandstone rocks and their mineral components during CO_2 injection in aquifers: Implications for fines migration. *J. Nat. Gas Sci. Eng.* **2020**, *73*, 103050.

(7) Galliero, G.; Volz, S. Thermodiffusion in model nanofluids by molecular dynamics simulations. *J. Chem. Phys.* **2008**, *128*, 064505−8.

(8) Li, Z.; Firoozabadi, A. Cubic-plus-association equation of state for water-containing mixtures: Is "cross association" necessary? *AIChE J.* **2009**, *55*, 1803−1813.

(9) De Groot, S.; Mazur, P. *Non-Equilibrium Thermodynamics*, 2nd ed.; Dover Publications: New York, 1984.

(10) Hirschfelder, J.; Bird, R. B.; Curtiss, C. F. *Molecular Theory of Gases and Liquids*; Wiley: New York, 1954.

(11) Firoozabadi, A. *Thermodynamics and Applications in Hydrocarbon Energy Production*, 1st ed.; McGraw-Hill Education: New York, 2016.

(12) Artola, P.; Rousseau, B. Thermal diffusion in simple liquid mixtures: What have we learnt from molecular dynamics simulations? *Mol. Phys.* **2013**, *111*, 3394−3403.

(13) Debuschewitz, C.; Köhler, W. Molecular Origin of Thermal Diffusion in Benzene+Cyclohexane Mixtures. *Phys. Rev. Lett.* **2001**, *87*, 055901−4.

(14) Hafskjold, B.; Ikeshoji, T.; Ratkje, S. K. On the molecular mechanism of thermal diffusion in liquids. *Mol. Phys.* **1993**, *80*, 1389−1412.

(15) Nieto-Draghi, C.; Ávalos, J. B.; Rousseau, B. Computing the Soret coefficient in aqueous mixtures using boundary driven nonequilibrium molecular dynamics. *J. Chem. Phys.* **2005**, *122*, 114503−7.

(16) Köhler, W.; Morozov, K. I. The Soret effect in liquid mixtures − A review. *J. Non-Equilib. Thermodyn.* **2016**, *41*, 151−197.

(17) Hoang, H.; Galliero, G. Predicting thermodiffusion in simple binary fluid mixtures. *Eur. Phys. J. E: Soft Matter Biol. Phys.* **2022**, *45*, 042−18.

(18) Windisch, C.; Maupin, G.; McGrail, B. Ultraviolet (UV) Raman spectroscopy study of the Soret effect in high-pressure CO_2-water solutions. *Appl. Spectrosc.* **2012**, *66*, 731−739.

(19) Guo, H.; Zhou, Q.; Wang, Z.; Huang, Y. Soret effect on the diffusion of CO_2 in aqueous solution under high-pressure. *Int. J. Heat Mass Transfer* **2018**, *117*, 966−971.

(20) Perronace, A.; Leppla, C.; Leroy, F.; Rousseau, B.; Wiegand, S. Soret and mass diffusion measurements and molecular dynamics simulations of n-pentane−n-decane mixtures. *J. Chem. Phys.* **2002**, *116*, 3718−3729.

(21) Mozaffari, S. H.; Srinivasan, S.; Ziad Saghir, M. Evaluations of molecular dynamics methods for thermodiffusion in binary mixtures. *J. Therm. Sci. Eng. Appl.* **2017**, *9*, 031011−9.

(22) Mozaffari, S. H.; Srinivasan, S.; Saghir, M. Z. Thermodiffusion in binary and ternary hydrocarbon mixtures studied using a modified heat exchange algorithm. *Therm. Sci. Eng. Prog.* **2017**, *4*, 168−174.

(23) Zhong, J.; Zhao, R.; Ouyang, W.; Xu, S. Molecular dynamics simulation of the Soret effect on two binary liquid solutions with equimolar n-alkane mixtures. *ACS Omega* **2022**, *7*, 518−527.

(24) Antoun, S.; Saghir, M. Z.; Srinivasan, S. An improved molecular dynamics algorithm to study thermodiffusion in binary hydrocarbon mixtures. *J. Chem. Phys.* **2018**, *148*, 104507–11.

(25) Simon, J. M.; Dysthe, D.; Fuchs, A.; Rousseau, B. Thermal diffusion in alkane binary mixtures: A molecular dynamics approach. *Fluid Phase Equilib.* **1998**, *150–151*, 151–159.

(26) Perronace, A.; Ciccotti, G.; Leroy, F.; Fuchs, A. H.; Rousseau, B. Soret coefficient for liquid argon-krypton mixtures via equilibrium and nonequilibrium molecular dynamics: A comparison with experiments. *Phys. Rev. E* **2002**, *66*, 031201–15.

(27) Miller, N. A. T.; Daivis, P. J.; Snook, I. K.; Todd, B. D. Computation of thermodynamic and transport properties to predict thermophoretic effects in an argon-krypton mixture. *J. Chem. Phys.* **2013**, *139*, 144504–10.

(28) Vaibhav, V.; Horbach, J.; Chaudhuri, P. Response of glassy liquids to thermal gradients. *Phys. Rev. E* **2020**, *101*, 022605–8.

(29) Hannaoui, R.; Galliero, G.; Hoang, H.; Boned, C. Influence of confinement on thermodiffusion. *J. Chem. Phys.* **2013**, *139*, 114704–7.

(30) Colombani, J.; Galliéro, G.; Duguay, B.; Caltagirone, J.-P.; Montel, F.; Bopp, P. A. A molecular dynamics study of thermal diffusion in a porous medium. *Phys. Chem. Chem. Phys.* **2002**, *4*, 313–321.

(31) Diaz-Marquez, A.; Stirnemann, G. Mass effects for thermodiffusion in dilute aqueous solutions. *Eur. Phys. J. E: Soft Matter Biol. Phys.* **2022**, *45*, 037.

(32) Diaz-Marquez, A.; Stirnemann, G. In silico all-atom approach to thermodiffusion in dilute aqueous solutions. *J. Chem. Phys.* **2021**, *155*, 174503–12.

(33) Rousseau, B.; Nieto-Draghi, C.; Avalos, J. B. The role of molecular interactions in the change of sign of the Soret coefficient. *Europhys. Lett.* **2004**, *67*, 976–982.

(34) Rezende Franco, L.; Sehnem, A. L.; Figueiredo Neto, A. M.; Coutinho, K. Molecular dynamics approach to calculate the thermodiffusion (Soret and Seebeck) coefficients of salts in aqueous solutions. *J. Chem. Theory Comput.* **2021**, *17*, 3539–3553.

(35) Römer, F.; Wang, Z.; Wiegand, S.; Bresme, F. Alkali halide solutions under thermal gradients: Soret coefficients and heat transfer mechanisms. *J. Phys. Chem. B* **2013**, *117*, 8209–8222.

(36) Di Lecce, S.; Albrecht, T.; Bresme, F. The role of ion–water interactions in determining the Soret coefficient of LiCl aqueous solutions. *Phys. Chem. Chem. Phys.* **2017**, *19*, 9575–9583.

(37) Di Lecce, S.; Bresme, F. Soret coefficients and thermal conductivities of alkali halide aqueous solutions via non-equilibrium molecular dynamics simulations. *Mol. Simul.* **2019**, *45*, 351–357.

(38) Noritake, F.; Kishi, T.; Yano, T. Relationship between Soret coefficient and potential energy distribution in silicate liquids: A molecular dynamics study. *J. Non-Cryst. Solids* **2019**, *525*, 119672–6.

(39) Müller-Plathe, F. A simple nonequilibrium molecular dynamics method for calculating the thermal conductivity. *J. Chem. Phys.* **1997**, *106*, 6082–6085.

(40) Wirnsberger, P.; Frenkel, D.; Dellago, C. An enhanced version of the heat exchange algorithm with excellent energy conservation properties. *J. Chem. Phys.* **2015**, *143*, 124104–8.

(41) Davidchack, R. L.; Handel, R.; Tretyakov, M. V. Langevin thermostat for rigid body dynamics. *J. Chem. Phys.* **2009**, *130*, 234101–14.

(42) Chen, X.; Liang, R.; Wang, Y.; Xia, Z.; Wu, L.; Liang, Y.; Cui, G. A theoretical study of the temperature gradient effect on the Soret coefficient in n-pentane/n-decane mixtures using non-equilibrium molecular dynamics. *J. Non-Equilib. Thermodyn.* **2020**, *45*, 319–332.

(43) Thompson, A. P.; Aktulga, H. M.; Berger, R.; Bolintineanu, D. S.; Brown, W. M.; Crozier, P. S.; in 't Veld, P. J.; Kohlmeyer, A.; Moore, S. G.; Nguyen, T. D.; et al. LAMMPS - A flexible simulation tool for particle-based materials modeling at the atomic, meso, and continuum scales. *Comput. Phys. Commun.* **2022**, *271*, 108171–34.

(44) Martin, M. G.; Siepmann, J. I. Transferable potentials for phase equilibria. 1. United-atom description of n-alkanes. *J. Phys. Chem. B* **1998**, *102*, 2569–2577.

(45) Peng, D.-Y.; Robinson, D. B. A new two-constant equation of state. *Ind. Eng. Chem. Fundamen.* **1976**, *15*, 59–64.

(46) Berendsen, H. J. C.; Grigera, J. R.; Straatsma, T. P. The missing term in effective pair potentials. *J. Phys. Chem.* **1987**, *91*, 6269–6271.

(47) Harris, J. G.; Yung, K. H. Carbon dioxide's liquid-vapor coexistence curve and critical properties as predicted by a simple molecular model. *J. Phys. Chem.* **1995**, *99*, 12021–12024.

(48) Vlcek, L.; Chialvo, A. A.; Cole, D. R. Optimized unlike-pair interactions for water–carbon dioxide mixtures described by the SPC/E and EPM2 models. *J. Phys. Chem. B* **2011**, *115*, 8775–8784.

(49) Potoff, J. J.; Siepmann, J. I. Vapor–liquid equilibria of mixtures containing alkanes, carbon dioxide, and nitrogen. *AIChE J.* **2001**, *47*, 1676–1682.

(50) Abascal, J. L. F.; Vega, C. A general purpose model for the condensed phases of water: TIP4P/2005. *J. Chem. Phys.* **2005**, *123*, 234505–12.

(51) Liu, Y.; Panagiotopoulos, A. Z.; Debenedetti, P. G. Monte Carlo simulations of high-pressure phase equilibria of CO_2–H_2O mixtures. *J. Phys. Chem. B* **2011**, *115*, 6629–6635.

(52) Orozco, G. A.; Economou, I. G.; Panagiotopoulos, A. Z. Optimization of intermolecular potential parameters for the CO_2–H_2O mixture. *J. Phys. Chem. B* **2014**, *118*, 11504–11511.

(53) Hockney, R. W.; Eastwood, J. W. *Computer Simulation Using Particles*, 1st ed.; IOP Publishing: London, 1988.

(54) Andersen, H. C. Rattle: A "velocity" version of the shake algorithm for molecular dynamics calculations. *J. Comput. Phys.* **1983**, *52*, 24–34.

(55) Kontogeorgis, G. M.; Voutsas, E. C.; Yakoumis, I. V.; Tassios, D. P. An equation of state for associating fluids. *Ind. Eng. Chem. Res.* **1996**, *35*, 4310–4318.

(56) Dawass, N.; Krüger, P.; Schnell, S. K.; Simon, J.-M.; Vlugt, T. Kirkwood-Buff integrals from molecular simulation. *Fluid Phase Equilib.* **2019**, *486*, 21–36.

(57) Tsivintzelis, I.; Kontogeorgis, G. M.; Michelsen, M. L.; Stenby, E. H. Modeling phase equilibria for acid gas mixtures using the CPA equation of state. Part II: Binary mixtures withCO_2. *Fluid Phase Equilib.* **2011**, *306*, 38–56.

(58) Kontogeorgis, G. M.; Michelsen, M. L.; Folas, G. K.; Derawi, S.; von Solms, N.; Stenby, E. H. Ten Years with the CPA (Cubic-Plus-Association) Equation of State. Part 1. Pure Compounds and Self-Associating Systems. *Ind. Eng. Chem. Res.* **2006**, *45*, 4855–4868.

(59) Perakis, C.; Voutsas, E.; Magoulas, K.; Tassios, D. Thermodynamic modeling of the vapor–liquid equilibrium of the water/ethanol/CO_2 system. *Fluid Phase Equilib.* **2006**, *243*, 142–150.

(60) Myint, P. C.; Hao, Y.; Firoozabadi, A. The CPA equation of state and an activity coefficient model for accurate molar enthalpy calculations of mixtures with carbon dioxide and water/brine. *arXiv* 2015; cond-mat.soft/1504, 05123-41 (accessed 2023-01-19).

(61) Riis, F.; Halland, E. CO_2 storage atlas of the Norwegian continental shelf: Methods used to evaluate capacity and maturity of the CO_2 storage potential. *Energy Procedia* **2014**, *63*, 5258–5265.

(62) Celia, M. A.; Bachu, S.; Nordbotten, J. M.; Bandilla, K. W. Status of CO_2 storage in deep saline aquifers with emphasis on modeling approaches and practical simulations. *Water Resour. Res.* **2015**, *51*, 6846–6892.

(63) Vishnyakov, A.; Weathers, T.; Hosangadi, A.; Chiew, Y. C. Molecular models for phase equilibria of alkanes with air components and combustion products I. Alkane mixtures with nitrogen, CO_2 and water. *Fluid Phase Equilib.* **2020**, *514*, 112553–11.

(64) Kobayashi, K.; Firoozabadi, A. Effect of branching on mutual solubility of alkane–CO_2 systems by molecular simulations. *J. Phys. Chem. B* **2022**, *126*, 8300–8308.

(65) Modig, K.; Pfrommer, B. G.; Halle, B. Temperature-dependent hydrogen-bond geometry in liquid water. *Phys. Rev. Lett.* **2003**, *90*, 075502–4.

(66) Danten, Y.; Tassaing, T.; Besnard, M. Infrared and molecular-dynamics studies of the rotational dynamics of water highly diluted in supercritical CO_2. *J. Chem. Phys.* **2005**, *123*, 074505–11.

(67) Gonçalves, A. F.; Castier, M.; Franco, L. F. The role of cross-association between carbon dioxide and hydrogen sulfide using the SAFT-VR Mie equation of state. *Fluid Phase Equilib.* **2022**, *559*, 113493−12.

(68) Bjørner, M. G.; Kontogeorgis, G. M. Modeling derivative properties and binary mixtures with CO_2 using the CPA and the quadrupolar CPA equations of state. *Fluid Phase Equilib.* **2016**, *408*, 151−169.

📖 Recommended by ACS

Even Strong Energy Polydispersity Does Not Affect the Average Structure and Dynamics of Simple Liquids

Trond S. Ingebrigtsen and Jeppe C. Dyre

MARCH 16, 2023
THE JOURNAL OF PHYSICAL CHEMISTRY B

READ 🗗

Charge Transport in Water–NaCl Electrolytes with Molecular Dynamics Simulations

Øystein Gullbrekken, Sondre Kvalvåg Schnell, *et al.*

MARCH 15, 2023
THE JOURNAL OF PHYSICAL CHEMISTRY B

READ 🗗

Interfacial Properties of Fluids Exhibiting Liquid Polyamorphism and Water-Like Anomalies

Thomas J. Longo, Frédéric Caupin, *et al.*

MARCH 23, 2023
THE JOURNAL OF PHYSICAL CHEMISTRY B

READ 🗗

Insulated Interlaced Surface Electrodes for Bacterial Inactivation and Detachment

Qiaoying Zhang, Chad D. Vecitis, *et al.*

MARCH 30, 2023
THE JOURNAL OF PHYSICAL CHEMISTRY B

READ 🗗

Get More Suggestions >